RSC Advances

PAPER

View Article Online
View Journal | View Issue

Cite this: *RSC Adv.*, 2015, **5**, 20858

Hofstadter spectra for d-orbital electrons: a case study on MoS_2

Yen-Hung Ho,[ab] Wu-Pei Su*[b] and Ming-Fa Lin*[c]

Received 26th November 2014
Accepted 13th February 2015

DOI: 10.1039/c4ra15271a

www.rsc.org/advances

To study the Hofstadter spectrum of monolayer molybdenum disulfide (MoS_2), we systematically examine the magnetic energy spectra due to various hoppings between d-orbital electrons to illustrate the link between the Bloch bands and the corresponding magnetoelectronic spectra. The magnetoelectronic spectrum shows a mirror (inversion) symmetry as a result of the particle–hole symmetry (asymmetry) in the Bloch bands. At small field, specific Landau fan diagrams can be ascribed to certain Bloch-band singularities. In the spectrum of real MoS_2, we further find a breaking of spectral symmetry, the spin and valley polarization, and a flux-dependent energy gap. Our numerical results can facilitate a qualitative understanding of the topological nature of d-bands and provide a basis for exploring the Landau levels in transition-metal dichalcogenides.

1 Introduction

Recent advances in the fabrication of two-dimensional (2D) materials leads to a renewal of interest in the Hofstadter spectrum.[1] In a magnetic field, Bloch bands are effectively converted into rich fractal butterfly patterns. Physically, it is a direct manifestation of the commensurability between atomic periodicity and magnetic vector potential. In recent experiments, the Hofstadter patterns have been observed on graphene superlattices, where the stacking twist significantly magnifies the lattice periodicity and thus enables the penetrating magnetic flux to reach the order of a flux quantum.[2–4] Accompanied by the rapid development of high magnetic field, the Hofstadter physics on atomically thin crystals has now become an object of intense investigation.

The Hofstadter spectra for various 2D lattice symmetries have been previously reported, such as the square lattice,[5–12] triangular lattice,[12,13] honeycomb lattice,[14–18] Kagome lattice,[19] and lattices in a modulated field,[20–23] where each atom contributes one orbital only. In this work, for a more realistic approach, we study the MoS_2 monolayer, where multiple orbitals per atom are taken into account. MoS_2 is one of the most stable 2D nanomaterials in the post-graphene era, which is also promising for spintronic and valleytronic applications due to its sizeable band gap and spin–orbit coupling. Therefore, the Hofstadter spectrum on such a realistic material has a great chance of being observed in future experiments.

Using a magnetic tight-binding model, we numerically compute the Hofstadter spectrum of MoS_2, as well as the spectra of involving hoppings between d orbitals. We clearly show how the 2D Bloch bands relate to the spectral symmetry and low-flux Landau level structures. In the MoS_2 spectrum, the site-energy difference results in the breaking of spectral symmetry, the spin–orbit coupling gives rise to the spin split, and the magnetic field leads to the valley split. The semiconductor–metal transition can be induced by tuning the penetrating flux.

2 Theoretical method

A MoS_2 monolayer consists of three atomic layers, a single layer of molybdenum atoms sandwiched between two layers of sulfur atoms. The main features of the Bloch bands in zero field are well described by density functional theory.[24–31] The low-energy electronic states are mainly dominated by the $4d_{z^2-r^2}$, $4d_{xy}$ and $4d_{x^2-y^2}$ orbitals of Mo atoms;[30–32] therefore, we have utilized a three-band model to study the Hofstadter spectra of MoS_2 where the parameters are fitted from the generalized gradient approximation.[32] The orbital geometry is shown in the inset of Fig. 1(a), where the three orbitals are respectively indexed by the magnetic quantum number $|m_l = 0\rangle$, $|-2\rangle$ and $|+2\rangle$. The molybdenum layer alone forms a 2D triangular lattice, and the primitive unit cell contains a single Mo atom. Each Mo atom interacts with six neighboring Mo atoms, where the lattice constant is $a = 3.19$ Å.

For the tight-binding electrons in a magnetic field $B\hat{z}$, a Peierls phase ΔG is implemented in the Hamiltonian matrix elements.[33–42] By choosing a Landau gauge with $\vec{A} = (0, Bx, 0)$,

[a]Department of Physics, National Tsing Hua University, Hsinchu 300, Taiwan
[b]Department of Physics and Texas Center for Superconductivity, University of Houston, Houston, Texas 77204, USA. E-mail: phys3z@central.uh.edu
[c]Department of Physics, National Cheng Kung University, Tainan 701, Taiwan. E-mail: mflin@mail.ncku.edu.tw

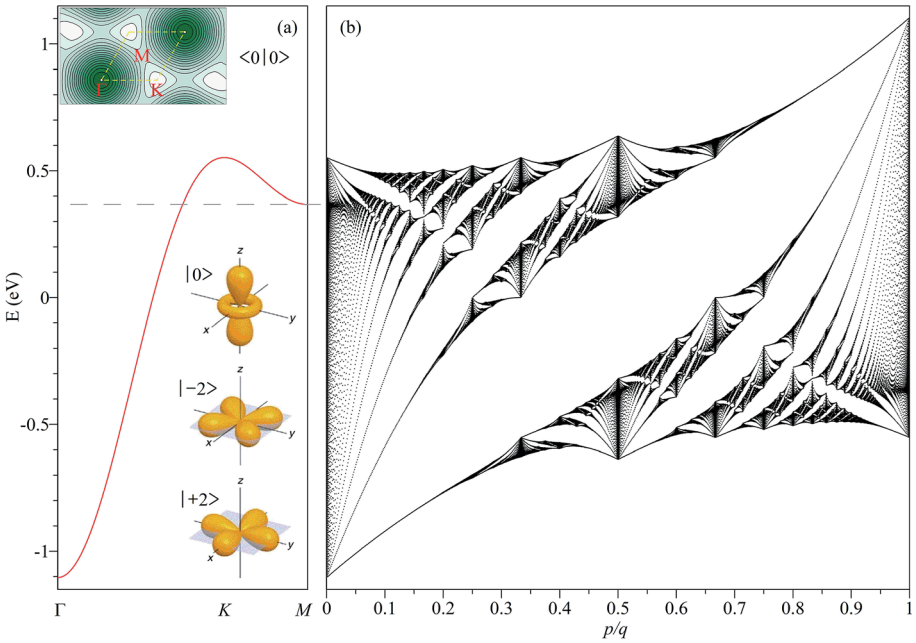

Fig. 1 (a) Zero-field Bloch band and (b) Hofstadter energy spectrum associated with the hopping between $|0\rangle$ orbitals of neighboring Mo atoms. In term of flux ratio p/q, we set $q = 797$ and vary p from 1 to q. The contour plot of (a) in momentum space is also shown in the inset.

this phase is given by the line integral of the vector potential as $\Delta G(\mathbf{R}_\alpha, \mathbf{R}_\beta) = \int_0^1 (\mathbf{R}_\alpha - \mathbf{R}_\beta)\cdot\mathbf{A}\left[\mathbf{R}_\beta + \lambda(\mathbf{R}_\alpha - \mathbf{R}_\beta)\right]\mathrm{d}\lambda$. To reach a flux quantum ϕ_0 per unit lattice cell, a magnetic field 2.3464×10^4 T is required.[33] Therefore, to satisfy the additional boundary condition due to a smaller magnetic field, the supercell is expanded to $m(=\phi_0/\phi)$-times larger. Accordingly, the wave function is expressed in the basis of $\{|0\rangle^j, |-2\rangle^j, |+2\rangle^j\}$ where $1 \le j \le m$. The solutions of this magnetic model cover the entire Brillouin zone.

3 Hopping between $|0\rangle$ orbitals

Considering the hopping between nearest neighboring $|0\rangle$ orbitals only, the tight-binding wave function is derived from the single orbital basis $|0\rangle$ and the Hamiltonian is given by[32]

$$H_{0,0} = 2t_0(\cos 2\alpha + 2\cos\alpha\cos\beta), \quad (1)$$

where $\alpha = \frac{1}{2}k_x a$ and $\beta = \frac{\sqrt{3}}{2}k_y a$. The hopping parameter is $t_0 = -0.184$ eV. The resulting 2D electronic structure is shown in Fig. 1(a), which is plotted along the highly symmetric points Γ, K and M in momentum space. For a better identification of the band features, a contour plot is also shown in the inset of Fig. 1(a). The Bloch band consists of a single band, which appears as local minimum at Γ point, local maximum at K point and saddle point at M point. It is also noted that the symmetry between the positive and negative energy is lacking. In what follows, we demonstrate that those band singularities are converted into specific fractal patterns in the magnetoelectronic spectra.

As a magnetic field applied normal to the surface, the Hamiltonian is given by[33]

$$H_{0,k;0,j} = t_0 e^{i2\alpha}\delta_{j,k-2} + 2t_0\cos\beta_j e^{i\alpha}\delta_{j,k-1} + t_0 e^{-i2\alpha}\delta_{j,k+2} + 2t_0\cos\beta_{j-1}e^{-i\alpha}\delta_{j,k+1}, \quad (2)$$

where j and k denote lattice sites within the magnetic supercell and $\cos\beta_j = \cos\left(\beta + \pi\frac{\phi}{\phi_0}\left(j + \frac{1}{2}\right)\right)$. The calculated Hofstadter spectrum is shown in Fig. 1(b). As a function of magnetic flux, the energy spectrum consists of self-similar recursive patterns: each parent band splits into multiple subbands which are also called daughter bands. When the flux ratio ϕ/ϕ_0 takes on a rational value p/q, the spectrum has a total of q Landau subbands. Here q and p are mutual primes and each Landau subband is p-fold degenerate. For a smaller q, Landau subbands tend to have broader band widths, implying that these magnetic subbands remain dispersive as a function of planar momentum. In the opposite limit, as q grows, the band widths quickly shrink. Eventually, Landau subbands turn into dispersionless Landau levels for a sufficient large q. Such a Hofstadter pattern is identical to that of simple triangular lattice which contains one orbital per atomic site.[12,13]

In the region of low magnetic flux, the Landau levels present certain fan-like structures. Each level has a specific field dependence that intimately relates to the band features in zero field. In going from the 2D Bloch band to the Landau levels, band around the local extrema turns into levels linear in flux. Alternatively, band around the saddle point turns into a cluster of Landau levels, as guided by the gray dashed lines in Fig. 1.

The butterfly spectral pattern can be characterized by an inversion symmetry about $E = 0$ and $p/q = 1/2$, indicating that the spectrum of $1/2 \leq p/q \leq 1$ equals to that of $0 \leq p/q \leq 1/2$ with a reversed energy. In other words, a reflection symmetry between positive and negative energy or between p/q and $1 - p/q$ does not exist. Such a lack of reflection symmetry in the Hofstadter spectrum can be ascribed to the absence of electron–hole symmetry of the Bloch band in zero field.

4 Hopping between $|0\rangle$ and $|\pm2\rangle$ orbitals

In zero field, the wave function is a linear combination of all the three orbital basis sets, *i.e.* $|0\rangle$, $|-2\rangle$ and $|+2\rangle$. The associated Hamiltonian matrix elements are described by[32]

$$\begin{aligned} H_{0,-2} &= -2\sqrt{3}t_2 \sin\alpha \sin\beta + 2it_1(\sin 2\alpha + \sin\alpha\cos\beta) \\ H_{0,+2} &= 2\sqrt{3}it_1 \cos\alpha \sin\beta + 2t_2(\cos 2\alpha - \cos\alpha\cos\beta). \end{aligned} \quad (3)$$

The relevant hopping parameters are $t_1 = 0.401$ eV and $t_2 = 0.507$ eV. As shown in Fig. 2(a), three Bloch bands appear. The centermost one is dispersionless and remains at $E = 0$. The other two bands are dispersive and have a reflection symmetry with respect to $E = 0$. In addition to the local extrema at M point and the saddle points in between Γ and K points, we also find pairs of linear bands intersecting at Γ and K points, forming Dirac cones. Furthermore, as the momentum moves away from the Dirac points, the isotropic subbands gradually involve into anisotropic ones. Those band singularities can be better identified from the energy contour plot shown in the inset of Fig. 2(a).

In the presence of a magnetic field, the Hamiltonian matrix elements are given by[33]

$$\begin{aligned} H_{0,k;-2,j} &= t_1 e^{i2\alpha}\delta_{j,k-2} + \left[t_1\cos\beta_j + \sqrt{3}it_2\sin\beta_j\right]e^{i\alpha}\delta_{j,k-1} \\ &\quad - t_1 e^{-i2\alpha}\delta_{j,k+2} + \left[-t_1\cos\beta_{j-1} - \sqrt{3}it_2\sin\beta_{j-1}\right]e^{-i\alpha}\delta_{j,k+1} \\ H_{0,k;+2,j} &= t_2 e^{i2\alpha}\delta_{j,k-2} + \left[-t_2\cos\beta_j + \sqrt{3}it_1\sin\beta_j\right]e^{i\alpha}\delta_{j,k-1} \\ &\quad + t_2 e^{-i2\alpha}\delta_{j,k+2} + \left[-t_2\cos\beta_{j-1} + \sqrt{3}it_1\sin\beta_{j-1}\right]e^{-i\alpha}\delta_{j,k+1}. \end{aligned} \quad (4)$$

In the computed Hofstadter spectrum shown in Fig. 2(b), one can find a reflection symmetry between electrons and holes, and also, in terms of the flux, a mirror symmetry between p/q and $1 - p/q$. Those symmetries can be ascribed to the e–h symmetry in zero field. In addition, for a given flux p/q, the number of Landau subbands is tripled to $3q$ since there are three Bloch bands in zero field. The $E = 0$ Landau level originated from the dispersionless Bloch band is field-independent. Other low-lying levels, in low-flux regime, are proportional to $\sqrt{B}$, in response to the linear bands intersecting at Γ and K points. In particular, some higher levels appear to form another fan diagram with a different field dependence. This feature is a direct consequence of the triangle warping. As illustrated in the inset of Fig. 2(a), such a warping effect is much stronger around K point compared to that around Γ point.

5 Hopping between $|\pm2\rangle$ orbitals

In the basis of $|-2\rangle$ and $|+2\rangle$, the associated Hamiltonian matrix elements are[32]

$$\begin{aligned} H_{-2,-2} &= 2t_{11}\cos 2\alpha + (t_{11} + 3t_{22})\cos\alpha\cos\beta \\ H_{+2,+2} &= 2t_{22}\cos 2\alpha + (3t_{11} + t_{22})\cos\alpha\cos\beta \\ H_{-2,+2} &= \sqrt{3}(t_{22} - t_{11})\sin\alpha\sin\beta + 4it_{12}\sin\alpha(\cos\alpha - \cos\beta), \end{aligned} \quad (5)$$

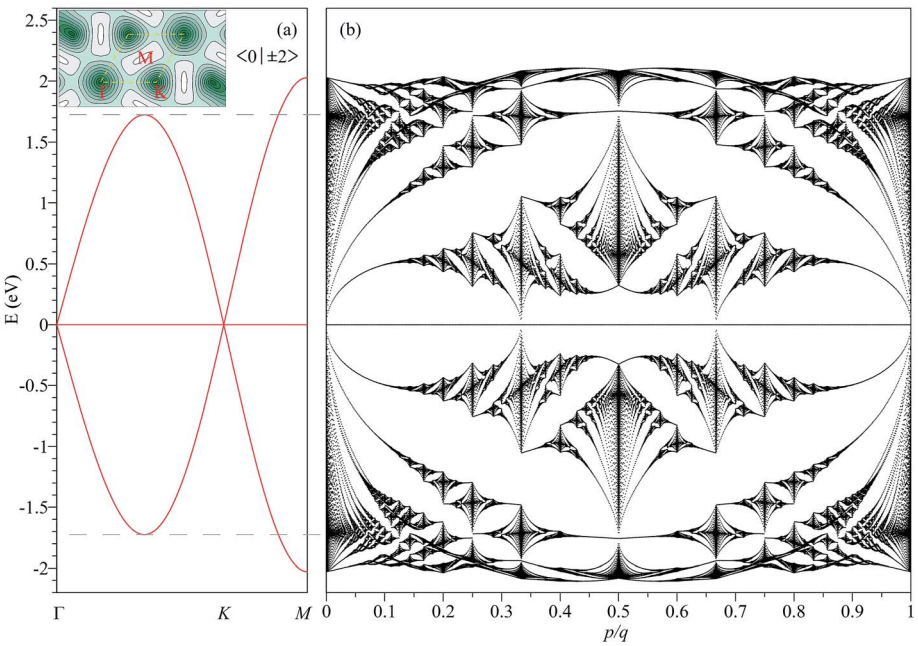

Fig. 2 Same plot as Fig. 1 but for the hoppings between $|0\rangle$ and $|\pm2\rangle$ orbitals. The inset of (a) is for the upper band.

where the hopping parameters involved are $t_{11} = 0.218$ eV, $t_{22} = 0.057$ eV and $t_{12} = 0.338$ eV. In a magnetic field, the Hamiltonian matrix elements become[33]

$$\begin{aligned}
H_{-2,k;j,-2} &= t_{11}e^{i2\alpha}\delta_{j,k-2} + \left[\frac{1}{2}(t_{11}+3t_{22})\cos\beta_j\right]e^{i\alpha}\delta_{j,k-1} \\
&\quad + t_{11}e^{-i2\alpha}\delta_{j,k+2} + \left[\frac{1}{2}(t_{11}+3t_{22})\cos\beta_{j-1}\right]e^{-i\alpha}\delta_{j,k+1} \\
H_{+2,k;j,+2} &= t_{22}e^{i2\alpha}\delta_{j,k-2} + \left[\frac{1}{2}(3t_{11}+t_{22})\cos\beta_j\right]e^{i\alpha}\delta_{j,k-1} \\
&\quad + t_{22}e^{-i2\alpha}\delta_{j,k+2} + \left[\frac{1}{2}(3t_{11}+t_{22})\cos\beta_{j-1}\right]e^{-i\alpha}\delta_{j,k+1} \\
H_{-2,k;j,+2} &= t_{12}e^{i2\alpha}\delta_{j,k-2} + \left[-i\frac{\sqrt{3}}{2}(t_{22}-t_{11})\sin\beta_j\right. \\
&\quad \left. -2t_{12}\cos\beta_j\right]e^{i\alpha}\delta_{j,k-1} - t_{12}e^{-i2\alpha}\delta_{j,k+2} \\
&\quad + \left[i\frac{\sqrt{3}}{2}(t_{22}-t_{11})\sin\beta_{j-1} + 2t_{12}\cos\beta_{j-1}\right]e^{-i\alpha}\delta_{j,k+1}.
\end{aligned} \tag{6}$$

Such a hopping leads to two Bloch bands with quite distinct topological nature, as shown in Fig. 3(a). As expected, the e–h asymmetry results in the inversion symmetry of the Hofstadter spectrum (Fig. 3(b)), analogous to the case of Fig. 1. Also, the counterparts of the band extrema and saddle points can be unambiguously found in the low-flux fan diagram, where the effect of triangular warping appears as the energy splitting of the first few top and bottom Landau levels.

6 Spin–orbit coupling

In general, an intrinsic spin–orbit coupling (SOC) exists in most transition-metal dichalcogenides. To address the spin degree of freedom, the basis is doubled to $|0,\uparrow\rangle$, $|-2,\uparrow\rangle$, $|+2,\uparrow\rangle$, $|0,\downarrow\rangle$, $|-2,\downarrow\rangle$, $|+2,\downarrow\rangle$. The Hamiltonian describing the SOC takes the form[32]

$$H' = \lambda\mathbf{L}\cdot\mathbf{S} = \frac{\lambda}{2}\begin{pmatrix} L_z & 0 \\ 0 & -L_z \end{pmatrix}, \tag{7}$$

where the coupling strength is $\lambda = 0.073$ eV for MoS_2. This coupling occurs between the $|-2\rangle$ and $|+2\rangle$ orbital states while the two states are of the same spin orientation. Note also that, such a SOC does not lead to spin flips. The strong spin–valley coupling in this system significantly suppresses the spin and valley relaxation, and thus the flip of spin and valley.[43] The spin-flip scattering may occur by introducing magnetic defects, which is beyond the scope of this study.

The energy spectrum with a nonzero t_{12} only is studied to elucidate the effect of SOC. Such a hopping is part of the hopping between the $|-2\rangle$ and $|+2\rangle$ orbitals. As the SOC is turned off, the zero-field Bloch band and the Hofstadter spectrum are shown as red curves in Fig. 4(a) and (b), respectively. All electronic states are doubly degenerate due to spin. In particular, the fractal butterfly spectrum coincides with the case of square lattice symmetry with one orbital per lattice site.[5–12] As the SOC applied, the spin degeneracy is effectively removed, as the blue curves shown in Fig. 4. More precisely, opposite spin states are shifted upward and downward by the same amount, which is $\lambda = 0.073$ eV.

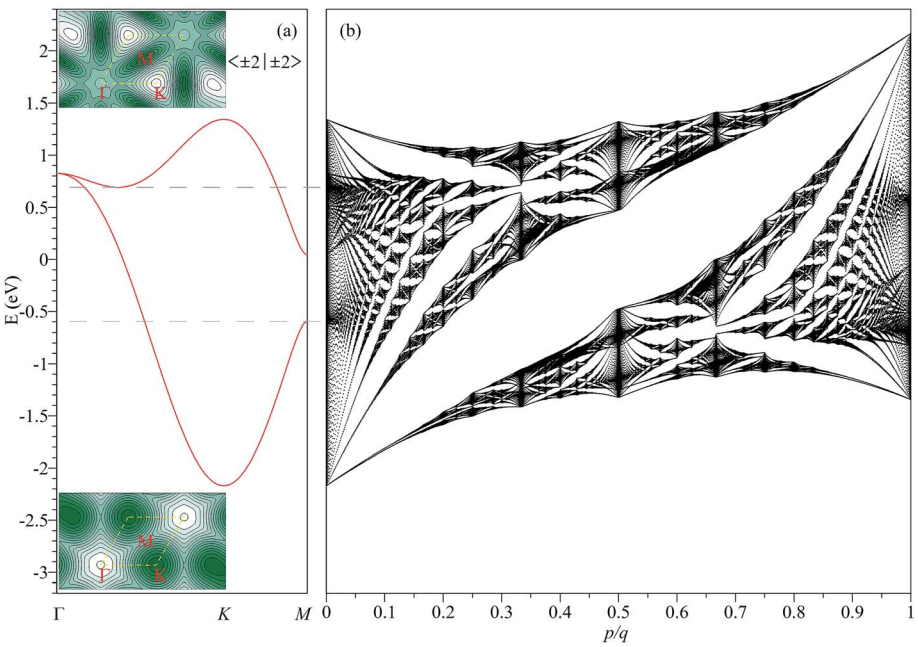

Fig. 3 Same plot as Fig. 1 but for the hoppings between $|\pm2\rangle$ orbitals. The top and bottom insets of (a) are for the upper and lower bands, respectively.

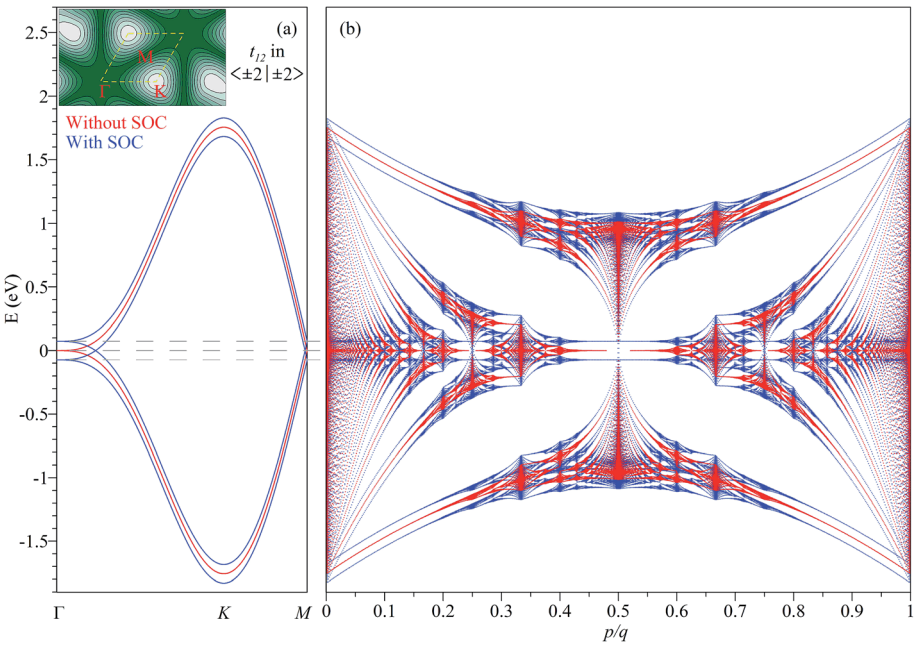

Fig. 4 Same plot as Fig. 1 but for t_{12} as the only non-zero hopping parameter. Spectra without and with SOC are colored red and blue, respectively.

7 Integrated spectrum

In the actual crystal field of MoS_2, one has to incorporate all the orbital hoppings and the SOC mentioned above. Furthermore, an on-site energy for each orbital has to be included in response to the real crystal field, which is $\varepsilon_1 = 1.046$ eV for the $|0\rangle$ orbital and $\varepsilon_2 = 2.104$ eV for the $|-2\rangle$ and $|+2\rangle$ orbitals.[32] These site energy terms, in the spectra of individual hoppings, give rise to an energy shift of entire electronic spectrum. The complete Hamiltonian in zero field therefore reads

$$\begin{pmatrix} H_{0,0}+\varepsilon_1 & H_{0,-2} & H_{0,+2} & 0 & 0 & 0 \\ H^*_{0,-2} & H_{-2,-2}+\varepsilon_2 & H_{-2,+2}+i\lambda & 0 & 0 & 0 \\ H^*_{0,+2} & H^*_{-2,+2}-i\lambda & H_{+2,+2}+\varepsilon_2 & 0 & 0 & 0 \\ 0 & 0 & 0 & H_{0,0}+\varepsilon_1 & H_{0,-2} & H_{0,+2} \\ 0 & 0 & 0 & H^*_{0,-2} & H_{-2,-2}+\varepsilon_2 & H_{-2,+2}-i\lambda \\ 0 & 0 & 0 & H^*_{0,+2} & H^*_{-2,+2}+i\lambda & H_{+2,+2}+\varepsilon_2 \end{pmatrix} \cdot (8)$$

The 2D Bloch bands are shown in Fig. 5(a). This system is a semiconductor with a direct energy gap of 1.59 eV bounded by the band edges at K point. The bottom of conduction band is composed of two bands that become degenerate right at K point. Upon a close examination of wave function, the two bands around the K point are found to be the spin-up and spin-down states of the $|0\rangle$ orbital, and thus labeled as $|0, \uparrow\rangle$ and $|0, \downarrow\rangle$, respectively. On the other hand, the top of valence band appears around K and Γ points. At Γ point, there are two degenerate bands, which are respectively the spin-up and spin-down states of the $|0\rangle$ orbital. As the momentum approaches K point, the two bands completely transform into $|\pm2\rangle$ orbital states and the two spin states here are widely split (the $|-2\rangle$ and $|+2\rangle$ states have the same behavior due to the same magnitude of magnetic quantum number, *i.e.*, $|m_l| = 2$). The removal of spin degeneracy in the K valley is a direct result of the intrinsic SOC. It is also worth mentioning that the two valence bands will interchange their spin orientation as the momentum moves to the neighboring K' valleys.

The Hofstadter spectrum of real MoS_2 is shown in Fig. 5(b), which reveals many intricate fractal structures. This spectrum in term of flux ceases to have a reflection symmetry or inversion symmetry. In fact, no apparent spectral symmetry can be concluded. The difference in on-site energy between the $|0\rangle$ and $|\pm2\rangle$ orbitals is the main reason. In low-flux regime, one can still relate the Landau fan diagram to specific Bloch-band singularities as elucidated above, including the linear field dependence and the clustering of Landau states. In this realistic spectrum, an energy gap exists, which monotonically decreases with increasing flux and closes at around $p/q = 1/3$. In particular, all the low-lying Landau levels shift away from the Fermi level except four of them moving toward the Fermi level. The four levels are respectively the threshold Landau levels quantized from the four low-lying subbands in the K valley. In Fig. 5(b) they are indexed as $|m_l, s, n\rangle_\tau = |0, \uparrow, 0\rangle_K$ and $|0, \downarrow, 0\rangle_K$ in the conduction band and $|\pm2, \downarrow, 0\rangle_K$ and $|\pm2, \uparrow, 0\rangle_K$ in the valence band. Here m_l stands for the orbital index, s for the spin index, n for the Landau index, and τ for the valley index. Such a characterization of Landau levels is in accord with the wave-function properties, which is detailed in ref. 33. Furthermore, some mixing of Landau levels can be found in a range of high flux (also in Fig. 2(b)), similar to the phenomenon reported in ref. 34.

The Landau level spectra in realistic magnetic field of 100 T are illustrated in Fig. 5(c) and (d), respectively for the bottom of conduction band and the top of valence band. Such a fan diagram can be linked to the hierarchy of quantum Hall states. Those

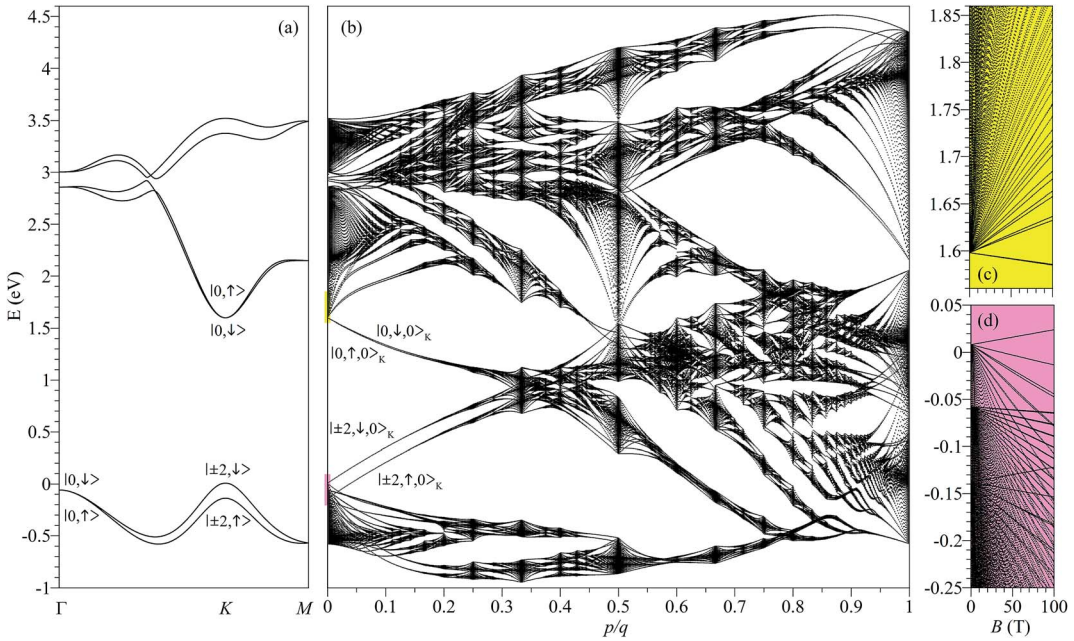

Fig. 5 (a) Zero-field Bloch bands and (b) Hofstadter energy spectrum incorporating all the orbital hoppings and the SOC mentioned above, as well as the on-site energies of the three orbitals. The Landau fan diagrams near the bottom of the conduction band and the top of the valence band are respectively plotted in (c) and (d) for a magnetic field up to 100 T.

Landau levels are all spin and valley polarized:[33] the spin splitting originates from the intrinsic SOC, while the valley splitting results from the inversion symmetry breaking of MoS_2 geometry caused by magnetic field. The conduction levels are magnetically condensed from the zero-field band edge at K point. The valence levels can be classified into three groups: the top and bottom groups come from the band edges at K point while the middle group from the band edge at Γ point. In addition, most levels appear in pairs, while in experiments the resolution of those pairs will require a low temperature and a high magnetic field.

8 Summary

In exploring the Hofstadter properties of MoS_2 monolayer, we systematically present the energy spectra due to various hoppings between 4d orbitals, and for each kind of hopping, we find the unique link between the Bloch bands and magnetoelectronic spectra. In particular, the particle–hole symmetry of Bloch band is responsible for the reflection symmetry in the Hofstadter spectrum. Moreover, in the range of low flux, Landau levels linear (square-root) in field are derived from the Bloch band near the parabolic band edge (Dirac point), while the cluster of Landau levels is derived from the band near the saddle point. In the integrated Hofstadter spectrum, the lift of spin degeneracy stems from the intrinsic SOC, and the breaking of inversion symmetry arises from the difference in on-site energy between orbitals. Such a case study on a realistic system can shed light on the topological features of d-electron-rich materials.

The Hofstadter spectra obtained by retaining part of hoppings between d orbitals can facilitate understanding the symmetry properties of individual hoppings. Even though those spectra do not directly correspond to the real MoS_2 one, in the future, they could still be realized in other possible 2D materials, which feature the low-lying subbands simply dominated by one of those orbital hoppings.

In the spectrum of real MoS_2, the low-flux fan diagram is of immediate experimental interest, which can be achieved in a suspended sample or samples barely coupled to the substrates and by using a continuous magnetic field (up to 45 T) and a non-destructive pulsed magnetic field (up to 100 T). In the range of higher flux, the Hofstadter spectrum is expected to observable in superlattice samples, as was done in graphene.[2–4] That is, a MoS_2 monolayer is commensurately coupled to the substrate, and the penetrating flux can be tuned by the twist angle. In this way, a modulation of energy gap, or even a semiconductor–metal transition, could be induced. A resolution of fractal patterns may require a fine tuning of the twist angle.

Acknowledgements

The authors thank Ming-Che Chang and Hong-Yi Chen for fruitful discussions. This work was supported by a start-up fund from NTHU, the Texas Center for Superconductivity, the Robert A. Welch Foundation under Grant no. E-1070, and the Ministry of Science and Technology of Taiwan under Grant no. NSC 102-2112-M-007-024-MY5 and NSC 101-2112-M-003-005-MY3.

References

1 D. Xiao, M.-C. Chang and Q. Niu, *Rev. Mod. Phys.*, 2010, **82**, 1959.

2 B. Hunt, J. D. Sanchez-Yamagishi, A. F. Young, M. Yankowitz, B. J. LeRoy, K. Watanabe, T. Taniguchi, P. Moon, M. Koshino, P. Jarillo-Herrero and R. C. Ashoori, *Science*, 2013, **340**, 1427.
3 C. R. Dean, L. Wang, P. Maher, C. Forsythe, F. Ghahari, Y. Gao, J. Katoch, M. Ishigami, P. Moon, M. Koshino, T. Taniguchi, K. Watanabe, K. L. Shepard, J. Hone and P. Kim, *Nature*, 2013, **497**, 598.
4 L. A. Ponomarenko, R. V. Gorbachev, G. L. Yu, D. C. Elias, R. Jalil, A. A. Patel, A. Mishchenko, A. S. Mayorov, C. R. Woods, J. R. Wallbank, M. Mucha-Kruczynski, B. A. Piot, M. Potemski, I. V. Grigorieva, K. S. Novoselov, F. Guinea, V. I. Fal'ko and A. K. Geim, *Nature*, 2013, **497**, 594.
5 D. R. Hofstadter, *Phys. Rev. B: Solid State*, 1976, **14**, 2239.
6 M.-C. Chang and Q. Niu, *Phys. Rev. Lett.*, 1995, **75**, 1348.
7 M.-C. Chang and Q. Niu, *Phys. Rev. B: Condens. Matter Mater. Phys.*, 1996, **53**, 7010.
8 M.-C. Chang and M.-F. Yang, *Phys. Rev. B: Condens. Matter Mater. Phys.*, 2002, **66**, 184416.
9 G. Gumbs, D. Miessein and D. Huang, *Phys. Rev. B: Condens. Matter Mater. Phys.*, 1995, **52**, 14755.
10 Q. W. Shi and K. Y. Szeto, *Phys. Rev. B: Condens. Matter Mater. Phys.*, 1997, **56**, 9251.
11 Y. Morita and Y. Hatsugai, *Phys. Rev. Lett.*, 2000, **86**, 151.
12 Y. Hatsugai and M. Kohmoto, *Phys. Rev. B: Condens. Matter Mater. Phys.*, 1990, **42**, 8282.
13 F. H. Claro and G. H. Wannier, *Phys. Rev. B: Condens. Matter Mater. Phys.*, 1979, **19**, 6068.
14 G. Gumbs and P. Fekete, *Phys. Rev. B: Condens. Matter Mater. Phys.*, 1997, **56**, 3787.
15 N. Nemec and G. Cuniberti, *Phys. Rev. B: Condens. Matter Mater. Phys.*, 2006, **74**, 165411.
16 N. Nemec and G. Cuniberti, *Phys. Rev. B: Condens. Matter Mater. Phys.*, 2007, **75**, 201404.
17 Y. Hatsugai, T. Fukui and H. Aoki, *Phys. Rev. B: Condens. Matter Mater. Phys.*, 2006, **74**, 205414.
18 M. Ezawa, *Sci. Rep.*, 2013, **3**, 3435.
19 Y. Xiao, V. Pelletier, P. M. Chaikin and D. A. Huse, *Phys. Rev. B: Condens. Matter Mater. Phys.*, 2003, **67**, 104505.
20 M.-C. Chang and M.-F. Yang, *Phys. Rev. B: Condens. Matter Mater. Phys.*, 1998, **57**, 13002.
21 M.-C. Chang and M.-F. Yang, *Phys. Rev. B: Condens. Matter Mater. Phys.*, 2004, **69**, 115108.
22 G. Gumbs, A. Iurov, D. Huang and L. Zhemchuzhna, *Phys. Rev. B: Condens. Matter Mater. Phys.*, 2014, **89**, 241407.
23 V. M. Apalkov and T. Chakraborty, *Phys. Rev. Lett.*, 2014, **112**, 176401.
24 D. Y. Qiu, F. H. da Jornada and S. G. Louie, *Phys. Rev. Lett.*, 2013, **111**, 216805.
25 T.-R. Chang, H. Lin, H.-T. Jeng and A. Bansil, *Sci. Rep.*, 2014, **4**, 6270.
26 W. Feng, Y. Yao, W. Zhu, J. Zhou, W. Yao and D. Xiao, *Phys. Rev. B: Condens. Matter Mater. Phys.*, 2012, **86**, 165108.
27 H. Shi, H. Pan, Y.-W. Zhang and B. I. Yakobson, *Phys. Rev. B: Condens. Matter Mater. Phys.*, 2013, **87**, 155304.
28 R. Das, B. Rakshit, S. Debnath and P. Mahadevan, *Phys. Rev. B: Condens. Matter Mater. Phys.*, 2014, **89**, 115201.
29 M. Gibertini, F. M. D. Pellegrino, N. Marzari and M. Polini, *Phys. Rev. B: Condens. Matter Mater. Phys.*, 2014, **90**, 245411.
30 Z. Y. Zhu, Y. C. Cheng and U. Schwingenschlogl, *Phys. Rev. B: Condens. Matter Mater. Phys.*, 2011, **84**, 153402.
31 J. E. Padilha, H. Peelaers, A. Janotti and C. G. Van de Walle, *Phys. Rev. B: Condens. Matter Mater. Phys.*, 2014, **90**, 205420.
32 G.-B. Liu, W.-Y. Shan, Y. Yao, W. Yao and D. Xiao, *Phys. Rev. B: Condens. Matter Mater. Phys.*, 2013, **88**, 085433.
33 Y.-H. Ho, Y.-H. Wang and H.-Y. Chen, *Phys. Rev. B: Condens. Matter Mater. Phys.*, 2014, **89**, 155316.
34 Y.-H. Ho, S.-J. Tsai, M.-F. Lin and W.-P. Su, *Phys. Rev. B: Condens. Matter Mater. Phys.*, 2013, **87**, 075417.
35 C. P. Chang, C. L. Lu, F. L. Shyu, R. B. Chen, Y. K. Fang and M. F. Lin, *Carbon*, 2004, **42**, 2975.
36 C. P. Chang, C. L. Lu, F. L. Shyu, R. B. Chen, Y. C. Huang and M. F. Lin, *Carbon*, 2005, **43**, 1424.
37 Y. H. Ho, J. Y. Wu, Y. H. Chiu, J. Wang and M. F. Lin, *Philos. Trans. R. Soc., A*, 2010, **368**, 5445.
38 Y. H. Lai, J. H. Ho, C. P. Chang and M. F. Lin, *Phys. Rev. B: Condens. Matter Mater. Phys.*, 2008, **77**, 085426.
39 Y.-H. Ho, Y.-H. Chiu, D.-H. Lin, C.-P. Chang and M.-F. Lin, *ACS Nano*, 2010, **4**, 1465.
40 Y. H. Ho, J. Wang, Y. H. Chiu, M. F. Lin and W. P. Su, *Phys. Rev. B: Condens. Matter Mater. Phys.*, 2011, **83**, 121201.
41 Y.-H. Ho, J.-Y. Wu, R.-B. Chen, Y.-H. Chiu and M.-F. Lin, *Appl. Phys. Lett.*, 2010, **97**, 101905.
42 Y.-H. Ho, Y.-H. Chiu, W.-P. Su and M.-F. Lin, *Appl. Phys. Lett.*, 2011, **99**, 011914.
43 D. Xiao, G.-B. Liu, W. Feng, X. Xu and W. Yao, *Phys. Rev. Lett.*, 2012, **108**, 196802.

